RESEARCH ARTICLE | AUGUST 25 2025

Implicit full-F simulations of neoclassical ion transport

M. Dorf ; M. Dorr ; D. Ghosh ; M. Umansky ; V. Soukhanovskii

Phys. Plasmas 32, 083904 (2025)
https://doi.org/10.1063/5.0280028
CHORUS

Implicit full-F simulations of neoclassical ion transport

Cite as: Phys. Plasmas **32**, 083904 (2025); doi: 10.1063/5.0280028
Submitted: 9 May 2025 · Accepted: 6 August 2025 ·
Published Online: 25 August 2025

M. Dorf,[a] M. Dorr, D. Ghosh, M. Umansky, and V. Soukhanovskii

AFFILIATIONS

Lawrence Livermore National Laboratory, Livermore, California 94550, USA

[a]Author to whom correspondence should be addressed: dorf1@llnl.gov

ABSTRACT

The development of implicit time integration capabilities for axisymmetric full-F continuum simulations of ion neoclassical transport is reported. The approach involves the implicit treatment of the gyrokinetic Vlasov equation coupled to the nonlinear Fokker–Planck collision model in the long-wavelength limit approximation. To facilitate implicit simulations, advanced preconditioning of individual physics operators is developed, and a global multi-physics preconditioner is constructed by adopting an operator splitting methodology. The algorithm is implemented in the finite-volume code COGENT and is applied to study neoclassical transport properties for both the main ion species and the lithium impurity species in the closed-field-line region of the LTX-β tokamak. The implicit COGENT simulations elucidate the role of non-local transport effects, while demonstrating substantial speedup over the corresponding explicit approach.

I. INTRODUCTION

Non-local ion kinetic effects play an important role in tokamak plasma transport when variations in background profiles are comparable to drift orbit excursions. This is often the case in the edge region, which is characterized by steep plasma gradients and moderate collisionality, allowing for the presence of wide banana orbits. Under such conditions, the background distribution can substantially deviate from a local Maxwellian, and a full-F kinetic (i.e., gyrokinetic) equation that includes a detailed collision operator must be solved to capture key features of plasma transport. Recognizing the importance of edge processes in achieving a steady state burning fusion plasma, the computational plasma physics community has been actively developing full-F edge gyrokinetic modeling capabilities over the last decade.[1–4] Such kinetic simulations are incredibly challenging due to their high dimensionality, the presence of multiple temporal and spatial scales, strong transport anisotropy, and complex divertor geometry involving a magnetic separatrix surface.

An analysis of ion kinetic effects can be facilitated by adopting a hybrid kinetic-fluid approach where the electron species is treated as a fluid.[4–9] Utilizing implicit time integration for a low-dimensional electron fluid system allows simulations to step over fast electron time scales. As a result, a significant speed-up over current state-of-the-art fully kinetic models can be achieved. Such hybrid implicit-explicit (IMEX) approach where a high-dimensional ion kinetic system is treated explicitly and a low-dimensional fluid electron system is handled implicitly is implemented in the finite-volume code COGENT for both 4D axisymmetric[8] and 5D turbulence[4,9] simulations of cross-separatrix plasma transport. While the ion parallel transit and collisional time scales have to be retained for adequate modeling of 5D ion-scale turbulence, axisymmetric (4D) simulations that primarily focus on quasi-stationary transport time scales can significantly benefit from stepping over these fast ion scales.

In this paper, we report on the development of implicit time integration capabilities for axisymmetric full-F continuum simulations of ion gyrokinetic transport with the COGENT code. Specifically, we discuss implicit treatment of the full-F gyrokinetic-Vlasov–Fokker–Planck (gVFP) equation in the long-wavelength limit approximation. To facilitate implicit simulations, advanced preconditioning of individual physics operators, such as Vlasov and nonlinear Fokker–Planck operators, is developed. The global multi-physics preconditioner for the entire gVFP operator is then constructed by adopting an operator splitting methodology. Notably, the preconditioning of the gyrokinetic Vlasov advection operator is distinguished by its use of highly efficient algebraic multigrid solvers contained in the Hypre linear solver library.[10] The use of multigrid methods to solve nonsymmetric indefinite systems, such as an advection equation, has historically been highly problematic, but the recent development of the Approximate Ideal Restriction approach[11,12] provides a way to extend the benefits of

multigrid algorithms beyond the symmetric, positive-definite systems for which they are more commonly used.

As an illustrative example, the COGENT simulation model is applied here to study neoclassical transport properties for both the main ion (hydrogen) and the lithium impurity species in the closed-field-line region of the Lithium Tokamak eXperiment-β[13,14] (LTX-β). Due to lithium's retention of hydrogen and its isotopes, a lithium-wall tokamak can exhibit reduced neutral production. This, in turn, can lead to lower temperature gradients from core to edge and mitigated temperature-driven anomalous transport. Under such conditions, neoclassical ion heat transport, driven by ion–ion collisions, may play a more significant role. Collisional particle transport of the lithium impurity species is also of considerable importance, as its accumulation in a tokamak core can lead to fuel dilution. Certain experimental scenarios (e.g., higher-recycling regime) on the LTX-β tokamak demonstrate the radial length scale of electron temperature variations in the edge region that can be the order of an ion banana width.[14] Although detailed ion temperature measurements are not available, non-local ion transport effect can become important if an ion temperature exhibits a similar profile.

The COGENT hybrid kinetic-ion/fluid-electron model for the simulations of hydrogen transport employs the long-wavelength limit of the full-F gyrokinetic equation coupled to the quasi-neutrality equation for electrostatic potential variations, $\nabla \cdot \mathbf{j} = 0$, where a fluid model is used for an electron response. For the highly conductive closed-field-line region of LTX-β, the hybrid model shows good agreement with the standard adiabatic, i.e., Boltzmann, electron model, which is often used to study neoclassical ion transport on closed field lines in both local and full-F simulations.[15–19] The adiabatic electron model, however, cannot be straightforwardly extended across the magnetic separatrix, in contrast to the hybrid model, which has been successfully used to study edge plasma transport in diverter geometries.[8]

To assess the role of a collisional model, three options for ion–ion collisions are compared: (i) the fully nonlinear Fokker–Planck operator,[20,21] (ii) a linearized model collisional operator,[19,22] and (iii) the Lenard–Bernstein/Dougherty (LBD) collision operator[23] that has often been employed in full-F gyrokinetic simulations.[2,9,24] Currently, only a linearized collision model is available in COGENT to describe multi-species collisions with a large mass difference, which is used here. This model preserves the dependence of the Coulomb mean free path on the relative velocity of the colliding species and has been verified to recover Braginskii's expression for the thermal and friction forces in a highly collisional regime.[25]

A substantial speed-up of numerical calculations can be obtained by utilizing implicit kinetic capabilities. In simulations of hydrogen neoclassical transport, the time step is, however, constrained by the timescale of collective electrostatic oscillations (e.g., geodesic acoustic modes) due to limitations of our numerical algorithms. This, in turn, can limit the advantage of using implicit time integration. In contrast, for impurity transport simulations that assume the trace limit with a fixed electric field, the full potential of the present implicit capabilities can be realized, and a speed-up of over 10× is demonstrated. The efficiency of the global multi-physics preconditioner is limited by the operator splitting approximation even if individual physics operators, i.e., the Vlasov operator and the Fokker–Planck operator, are well preconditioned. Note that for the case of the LTX-β system modeled here, the Courant-limited time steps corresponding to the advection and collision operators are of the same order. Therefore, larger speed-up factors can be expected when modeling physical systems in which stiffness is dominated by a single term. For instance, this could occur in (i) edge modeling, where cold regions near target plates make collisional processes the dominant source of stiffness, or (ii) weakly collisional transport in a hot core, where stiffness is primarily governed by the advection operator.

The present paper is organized as follows. The simulation model is described in Sec. II. The results of numerical simulations for the neoclassical transport of the main ion (hydrogen) and impurity (lithium) species are presented in Secs. III and IV, respectively. Finally, the conclusions of the present work are summarized in Sec. V.

II. SIMULATION MODEL

A. Model equations

The neoclassical simulations presented in this work use the 4D axisymmetric version of the COGENT code that solves the long-wavelength limit of a full-F ion gyrokinetic equation written in a conservative form

$$\frac{\partial (B^*_{\parallel i} f_i)}{\partial t} + \nabla \cdot \left(\dot{\mathbf{R}}_i B^*_{\parallel i} f_i \right) + \frac{\partial}{\partial v_\parallel} \left(\dot{v}_{\parallel i} B^*_{\parallel i} f_i \right) = C\left[B^*_{\parallel i} f_i \right]. \tag{1}$$

Here, $f_i(\mathbf{R}, v_\parallel, \mu)$ denotes the ion gyroaveraged distribution function, ∇ is the gradient with respect to $\mathbf{R}$, and the phase-space guiding-center velocities are given by

$$\dot{\mathbf{R}}_i = \frac{1}{B^*_{\parallel i}} \left[v_\parallel \mathbf{B}^* + \frac{c}{Z_i e} \mathbf{b} \times (Z_i e \nabla \Phi + \mu \nabla B) \right], \tag{2}$$

$$\dot{v}_{\parallel i} = -\frac{1}{m_i B^*_{\parallel i}} \mathbf{B}^* \cdot (Z_i e \nabla \Phi + \mu \nabla B), \tag{3}$$

where m_i and Z_i are the ion species mass and charge state, respectively, e is the elementary charge, c is the speed of light, $\mathbf{B} = B \cdot \mathbf{b}$ is the magnetic field with $\mathbf{b}$ denoting the unit vector along the field, $\mathbf{B}^*_i(\mathbf{R}, v_\parallel) \equiv \mathbf{B} + (c m_i / Z_i e) v_\parallel \nabla \times \mathbf{b}$, $B^*_{\parallel i} = \mathbf{B}^*_i \cdot \mathbf{b}$, and the long-wavelength limit, $k_\perp \rho_i \ll 1$, is presently adopted for electrostatic potential variations, $\Phi(\mathbf{R}, t)$, and collision models, $C[B^*_{\parallel i} f_i]$. Here, $\rho_i = V_{Ti}/\Omega_i$ is the particle thermal gyroradius, $V_{Ti} = \sqrt{2T_i/m_i}$ is the thermal velocity, $\Omega_i = Z_i e B/(m_i c)$ is the cyclotron frequency, and $k_\perp^{-1}$ represents the characteristic length-scale for variations in the electrostatic potential and distribution function perturbations. To assess the role of a collisional model, three options are used to describe self-hydrogen collisions: (i) the fully nonlinear Fokker–Planck operator,[20,21] (ii) a linearized model collisional operator,[19,22] and (iii) the Lenard–Bernstein/Dougherty (LBD) collision operator[23] that is often employed in full-F gyrokinetic simulations.[2,9,24] To describe collisions between the lithium and hydrogen species, a linearized multi-species collision model is used.[25]

The hybrid kinetic-ion/fluid-electron model describes the self-consistent evolution of electrostatic potential perturbations by solving the quasi-neutrality equation ($\nabla \cdot \mathbf{j} = 0$) for the vorticity variable[4]

$$\varpi = \nabla_\perp \cdot \left(\sum_i \frac{c^2 n_i m_i}{B^2} \nabla_\perp \Phi \right), \tag{4}$$

coupled to a fluid model for an electron response

$$\frac{\partial \varpi}{\partial t} = \nabla \cdot \left(\sum_i \frac{2\pi Z_i e}{m_i} \int dv_\parallel d\mu \mathbf{v}_{i\perp}^m f_i B_{\parallel i}^* \right) + \nabla \cdot \left[\frac{c n_e T_e}{B} \left(\nabla \times \mathbf{b} + \frac{\mathbf{b} \times \nabla B}{B} \right) \right] + B \nabla_\parallel \left[\frac{\sigma_\parallel}{B} \left(\frac{1}{e n_e} \nabla_\parallel (n_e T_e) - \nabla_\parallel \Phi + \frac{0.71}{e} \nabla_\parallel T_e \right) \right]. \quad (5)$$

Here, $\nabla_\perp \equiv \nabla - \mathbf{b}(\mathbf{b} \cdot \nabla)$ is the perpendicular gradient operator, $\mathbf{v}_{i\perp}^m \equiv \dot{\mathbf{R}}_{i\perp}(\Phi = 0)$ is the magnetic drift velocity corresponding to the perpendicular component of the guiding center velocity in Eq. (2) for the case of a zero potential, $\sigma_\parallel = 1.96 n_e e^2 \tau_e / m_e$ is the parallel electron conductivity, with τ_e denoting the basic electron collisional term given by Braginskii,[26] and T_e is the electron temperature. For the case of long-wavelength axisymmetric transport modeling we neglect the diamagnetic corrections, $\sim cB^{-1}\Omega_i^{-1}\Delta_\perp p_i$, on the RHS of Eq. (4) as well as the Reynolds-stress term and the polarization density correction terms on the RHS of Eq. (5), assuming

$$n_e = \sum_i Z_i n_i = \sum_i Z_i \frac{2\pi}{m_i} \int dv_\parallel d\mu f_i B_{\parallel i}^*. \quad (6)$$

Equations (4)–(6) represent the COGENT vorticity model for self-consistent variations of the electrostatic potential that needs to be coupled with a model for an electron temperature. For simplicity, here we consider a fixed electron temperature distribution, $T_e(\mathbf{R}, t) = T_e(\psi)$, which is assumed to be uniform on magnetic flux surfaces, ψ.

In a highly conductive limit, the vorticity model in Eq. (5) is consistent with the adiabatic electron model that is often used in the simulations of long-wavelength neoclassical transport[15–19] and ITG turbulence[27,28] in a tokamak core region,

$$\nabla_\perp \cdot \left(\sum_i \frac{c^2 m_i n_i}{B^2} \nabla_\perp \Phi \right) = e \left(n_e - \sum_i Z_i n_i \right), \quad (7)$$

where

$$n_e = (1 + e\Phi/T_e - e\langle \Phi \rangle / T_e) n_{e0} \ . \quad (8)$$

Here, $\langle Q \rangle$ is the flux-surface average defined as the volume average of Q between two neighboring flux surfaces, ψ and $\psi + d\psi$, and $n_{e0} = \sum_i Z_i n_{i0}$ corresponds to the density of a fixed local-Maxwellian background. The consistency between the two models can be shown as follows: In the long-wavelength limit, we can neglect the contribution of the polarization density term on the LHS of Eq. (7) to the poloidal variations of the electrostatic potential, which are then given by the Boltzmann response, $e\delta\Phi/T_e \approx (n_e - n_{e0})/n_{e0}$. The same result follows from the vorticity model in Eq. (5) assuming large values of the parallel conductivity and small-amplitude density perturbations. Then, the consistency of the solution for $\langle \Phi \rangle$ in the two models can be demonstrated by taking the time derivative of the flux-surface-averaged Eq. (7) and comparing it with the flux-surface average of Eq. (5). For the latter calculation, one can adopt the following useful relationships: $\langle B \nabla_\parallel (\ldots) \rangle = 0$, $\nabla \cdot \left[\frac{p_e}{B} \left(\nabla \times \mathbf{b} + \frac{\mathbf{b} \times \nabla B}{B} \right) \right] = \nabla \cdot \left(- \frac{\nabla_\perp p_e \times \mathbf{b}}{B} \right)$, and $\left\langle \nabla \cdot \left(- \frac{\nabla_\perp p_e \times \mathbf{b}}{B} \right) \right\rangle \approx \left\langle \nabla \cdot \left(- e n_e \frac{\nabla_\perp \Phi \times \mathbf{b}}{B} \right) \right\rangle$. In obtaining the last relationship, we made use of the Boltzmann response for poloidal variations of the electrostatic potential, $\delta\Phi$. Finally, we note that although the adiabatic electron model is simpler to implement and solve, it cannot be straightforwardly extended across the magnetic separatrix.[4] In contrast, the hybrid model has been successfully used to study edge plasma transport in divertor geometries with both 4D axisymmetric[8] and 5D turbulence[4,9] versions of the COGENT code.

B. Boundary conditions

The phase-space advection operator in the ion gyrokinetic equation [Eq. (1)] requires specification of "inflow" fluxes at the phase-space boundaries. Two types of simulations are performed in this work, for which we use different sets of boundary conditions. The simulations of hydrogen transport are performed on a short (collisional) time scale to evaluate neoclassical heat fluxes corresponding to given background plasma profiles. Here, it is instructive to note that using the standard gyrokinetic model on longer (transport) time scales has limited validity (e.g., for a background electric field) unless non-intrinsically ambipolar processes are present.[29,30] For the hydrogen simulations, the inflow fluxes are computed from the initial locally Maxwellian distribution and they are maintained fixed throughout the simulation.

Trace lithium simulations, which assume a fixed hydrogen background and a fixed electrostatic potential distribution, are performed over a long transport time scale until the impurity species profiles reach saturation. These simulations utilize an *ad hoc* flux-driven radial boundary condition, in which inflow phase-space fluxes are adjusted at each time step to maintain prescribed values of the total (i.e., combined inflow and outflow) radial fluxes of particles, heat, and angular momentum. In more detail, the inflow distribution function is assumed to have the following form at a radial boundary

$$f_{BC}^{in} = F_M \left(\overline{n}, \overline{V}_\parallel, \overline{T} \right) \left[1 + \frac{\delta n}{\overline{n}} + \frac{m \left(v_\parallel - \overline{V}_\parallel \right)}{\overline{T}} \delta V_\parallel + \left(\frac{m \left(v_\parallel - \overline{V}_\parallel \right)^2}{2\overline{T}} + \frac{\mu B}{\overline{T}} - \frac{3}{2} \right) \frac{\delta T}{\overline{T}} \right]. \quad (9)$$

Here, F_M denotes a Maxwellian distribution, and $\overline{n}$, $\overline{V}_\parallel$, and $\overline{T}$ are the scalar values corresponding to the poloidally averaged density, parallel velocity, and temperature moments of the distribution function, f_{bnd}^{out}, which is extrapolated from the interior to the radial boundary of the simulation domain and describes the outflow fluxes. Note that the distribution function in Eq. (9) corresponds to the linearization of $F_M(\overline{n} + \delta n, \overline{V}_\parallel + \delta V_\parallel, \overline{T} + \delta T)$. At each time step, the scalar perturbations δn, $\delta V_\parallel$, and δT are found from the following linear system:

$$\Lambda_n^{in} = \oint dA \int \int_{V_{dr}^{in}} dv_\parallel d\mu \frac{2\pi}{m} |\dot{\mathbf{R}} \cdot \mathbf{e}_\psi| K_n B_\parallel^* f_{BC}^{in} - \oint dA \int \int_{V_{dr}^{out}} dv_\parallel d\mu \frac{2\pi}{m} |\dot{\mathbf{R}} \cdot \mathbf{e}_\psi| K_n B_\parallel^* f_{bnd}^{out}. \quad (10)$$

Here, Λ_n^{in} denotes the inward radial fluxes of particle ($n = 1$), angular momentum ($n = 2$), and energy ($n = 3$) integrated over the flux-surface area with an area element, dA. The corresponding kernel functions are given by $K_1 = 1$, $K_2 = m(I/B)v_\parallel$, and $K_3 = m v_\parallel^2/2 + \mu B + Ze\Phi$. The velocity integral limits $V_{dr}^{in}(V_{dr}^{out})$ select particles with drift velocities $V_{dr} = \dot{\mathbf{R}} \cdot \mathbf{e}_\psi$ directed inside (outside) the

simulation domain, $\mathbf{e}_\psi$ is the unit vector normal to a magnetic flux surface, directed outward, and the subscript i (denoting ions) is suppressed to simplify notation. The constraints in Eq. (10) enforce matching of the total fluxes of the particle, angular momentum, and energy through a radial boundary with the prescribed values, Λ_n^{in}. In particular, a zero particle flux boundary condition is used in the simulations of lithium transport at the inner radial boundary to compensate for the fact that the COGENT simulation domain cannot be extended all the way to the magnetic axis.

Available radial boundary conditions for a potential include the standard Dirichlet and Neumann conditions as well as the "consistent" condition that can be applied on the radial closed-flux-surface boundaries:[4,8]

$$\left\langle \sum_i \frac{c^2 n_i m_i}{B^2} |\nabla\psi|^2 \right\rangle \frac{\partial \Phi}{\partial \psi} = \sum_i \int_0^t dt \langle \nabla\psi \cdot \mathbf{j}_i \rangle. \tag{11}$$

The constraint in Eq. (11) enforces the balance between the total charge carried through the radial boundary by the neoclassical ion current and the polarization current. This consistent condition enables numerical solutions with a non-vanishing E_r at the inner radial boundary and alleviates the need for radial buffer regions. Such regions are often included in global simulations that employ standard zero-Neumann conditions and use buffer zones to diffuse profile gradients. Finally, imposing the boundary condition in Eq. (11) on both the inner and outer radial boundaries in the case of annular geometry ensures that Eqs. (7) and (8) have a valid solution. Note that imposing zero-Neumann boundary conditions on both radial boundaries would require artificially maintaining zero total (i.e., volume-integrated) charge for the solvability of the adiabatic electron model in Eqs. (7) and (8).

C. Numerical implementation

The hybrid kinetic-ion/fluid-electron simulation model is solved in the COGENT code using the additive Runge–Kutta (ARK) implicit–explicit (IMEX) approach,[21] which provides consistent time integration up to fourth order in Δt while treating selected stiff terms implicitly. This scheme has been successfully applied to the modeling of ion-scale turbulence, where the explicit 5D ion gyrokinetic equation is coupled with the 3D implicit field/fluid model.[31] Here, to simplify the computationally expensive implicit solution of the Vlasov operator, we take an electrostatic field to be fixed during an IMEX time step update of the ion gyrokinetic equation. The field is only updated at the end of a step by solving Eq. (5). Although such assumption reduces the time integration accuracy of the hybrid kinetic-fluid system, its impact may be minimal for neoclassical transport simulations that focus on quasi-stationary solutions. It is, however, instructive to note that the fixed E-field approximation may limit the stability of our IMEX approach for stepping over collective electrostatic oscillations, such as geodesic acoustic modes (GAMs). The implementation of the nonlinear Fokker–Planck operator is similarly simplified by keeping the Rosenbluth potentials fixed during a time step. In this case, the implicit collision operator becomes "mathematically" linear in the equation governing the implicit time step advance.

Under the fixed electric field/Rosenbluth potential approximation, a linear implicit system derived from the gyrokinetic Vlasov–Fokker–Planck equation is solved using the Generalized Minimal Residual (GMRES) method.[32] To facilitate the linear solve, COGENT employs a multi-physics preconditioning framework. In this approach, a global preconditioner is constructed by combining individual preconditioners, each developed separately for distinct physics terms, using the operator-splitting methodology

$$I - \alpha\Delta t \sum_k J_k \approx \prod_k (I - \alpha\Delta t J_k). \tag{12}$$

Here, J_k represents different physics operators, e.g., the gyrokinetic Vlasov and the Fokker–Planck operators, and α is a constant coefficient dependent on the order of the ARK scheme and the stage number. The right-hand side of Eq. (12) is used for global preconditioning, which corresponds to the sequential application of individual preconditioner operators. Notably, inverting the operator on the right-hand side of Eq. (12) simply implies the consecutive inversion of the individual preconditioners.

The individual preconditioner operators for the collisional and the gyrokinetic Vlasov terms are constructed as follows: The development of preconditioning for the implicit treatment of the Fokker–Planck operator is described in detail in Ref. 21. It is based on a lower-order velocity-space discretization of the operator, with the resulting sparse matrix inverted using the Gauss–Seidel method. The same methodology is used to precondition the LBD collision operator and the stiff test-particle term of the linearized multi-species collision operator. The latter collision model is used in the implicit simulations of the lithium impurity species transport.

Efficient preconditioning of the Vlasov operator requires solving a linear system in the full phase space dimension with a non-symmetric and indefinite coefficient matrix. COGENT solves this linear system using the Approximate Ideal Restriction (AIR) option in the BoomerAMG algebraic multigrid solver contained in the Hypre linear solver library.[10] The use of multigrid methods to solve nonsymmetric indefinite systems has historically been highly problematic, but the recent development of the AIR approach, including several variants, provides a way to extend the benefits of multigrid algorithms beyond the symmetric, positive-definite systems for which they are more commonly used.[11,12] To further enhance the efficiency and robustness of the implicit Vlasov solver, COGENT allows the preconditioner to be defined using a lower-order discretization than that used for the Vlasov operator itself. To achieve high-order spatial accuracy, higher-order upwind schemes (here, third-order) are routinely employed to discretize the Vlasov operator. The preconditioner, is however, typically constructed using a first-order upwind scheme (UW1). The low-order preconditioner yields a sparser matrix, for which robust AMG solver performance is observed, while also providing efficiency even for relatively large time steps.

An electrostatic potential in the hybrid kinetic-ion/fluid-electron system is determined from the vorticity model in Eq. (5) that contains fast electron time scales associated with high plasma conductivity, $\tau_{cond} \sim (k_\perp^2/k_\parallel^2)(c^2 \sum_i n_i m_i/(\sigma_\parallel B^2))$. Although in axisymmetric simulations the ratio of the perpendicular to parallel wave-vectors in potential perturbations is bounded by $k_\perp/k_\parallel \gtrsim B/B_\theta$, this time scale is nevertheless much faster than the ion cyclotron time period for typical tokamak parameters. For instance, for the parameters characteristic of LTX-β, $n_e \sim 10^{13}\,\mathrm{cm}^{-3}$, $T_e \sim 100\,\mathrm{eV}$, $B/B_\theta \sim 4$ we obtain $\tau_{cond}\omega_{ci} \sim 10^{-4}$. Therefore, the electrostatic vorticity model must be treated implicitly.

In the present work, a simple first-order backward Euler method is used to find an electrostatic potential solution at the end of a time step

$$\nabla_\perp \cdot \left(\frac{c^2 \sum_i m_i n_i}{B^2} \nabla_\perp \frac{\Phi^{l+1} - \Phi^l}{\Delta t} \right) + B\nabla_\parallel \left(\frac{\sigma_\parallel}{B} \nabla_\parallel \Phi^{l+1} \right) = RHS. \quad (13)$$

Here, Δt is a time step size and the RHS of Eq. (13) represents all remaining terms in Eq. (5). The ion density and the RHS terms are evaluated from the ion distribution function at the end of the lth time step. The solution of the strongly anisotropic elliptic operator in Eq. (13) is facilitated by making use of parallel algebraic multigrid (AMG) solvers contained in the Hypre library.[10] Finally, we note that the time-dependent boundary condition in Eq. (11) is updated explicitly in time.

The IMEX hybrid model [in Eqs. (1) and (5)] is verified against the fully explicit adiabatic electron model [in Eqs. (1), (7), and (8)], for which developing an efficient approach to solving the field equations [Eqs. (7) and (8)] is necessary. Although COGENT offers various methods for handling sparsely coupled elliptic equations, the presence of the flux-surface averaged potential on the right-hand side of Eq. (8)—which governs the evolution of the radial electric field—introduces dense (long-range, non-local) coupling. To address this, COGENT employs "sub-space" iterations, where the flux-surface averaged component, $\langle \Phi \rangle$, and the poloidally varying component, $\delta\Phi = \Phi - \langle \Phi \rangle$, are solved alternately. These components belong to orthogonal functional subspaces, and the iterations continue until the combined solution satisfies the original gyrokinetic Poisson equation. Further details of this approach can be found in Ref. 4.

III. SIMULATIONS OF THE HYDROGEN NEOCLASSICAL TRANSPORT

Here, we present the results of full-F COGENT simulations of hydrogen neoclassical transport for parameters characteristic of the LTX-β experiment. The magnetic geometry used in the simulations is shown in Fig. 1. The poloidal magnetic flux function, ψ, is obtained by performing axisymmetric free-boundary equilibrium reconstructions of tokamak plasmas using the PSI-Tri equilibrium code.[33] The toroidal magnetic field is specified by $RB_\phi = const$, with the on-axis magnetic field given by $B_0 = 3$ kG. Here, R is the major radius coordinate. A coarse version of the flux-aligned COGENT grid is illustrated in Fig. 1(a). The grid is chosen to be non-orthogonal in order to minimize non-uniformities in the poloidal cell size. COGENT simulations ignore the presence of the limiter wall and span the radial region of $\psi_N = (0.15; 1.1)$. Here, $\psi_N = (\psi - \psi_{axis})/(\psi_{LCFS} - \psi_{axis})$ is the normalized poloidal magnetic flux function with ψ_{axis} and ψ_{LCFS} denoting the poloidal flux values at the magnetic axis and the last closed flux surface, respectively. The annular geometry is artificially extended beyond the last closed flux surface to reduce the influence of boundary conditions imposed at the outer radial boundary. For the same reason, the characteristic LTX-β background plasma profiles for the plasma density and electron temperature,[14] which are used for initialization, are arbitrarily flattened in the near-boundary region, $\psi_N > 0.9$. To demonstrate the efficiency of the implicit algorithms, a higher-recycling regime with stronger temperature variations and higher collisionality is considered.[14] The initial ion temperature is assumed to be half of the electron temperature.[13,14]

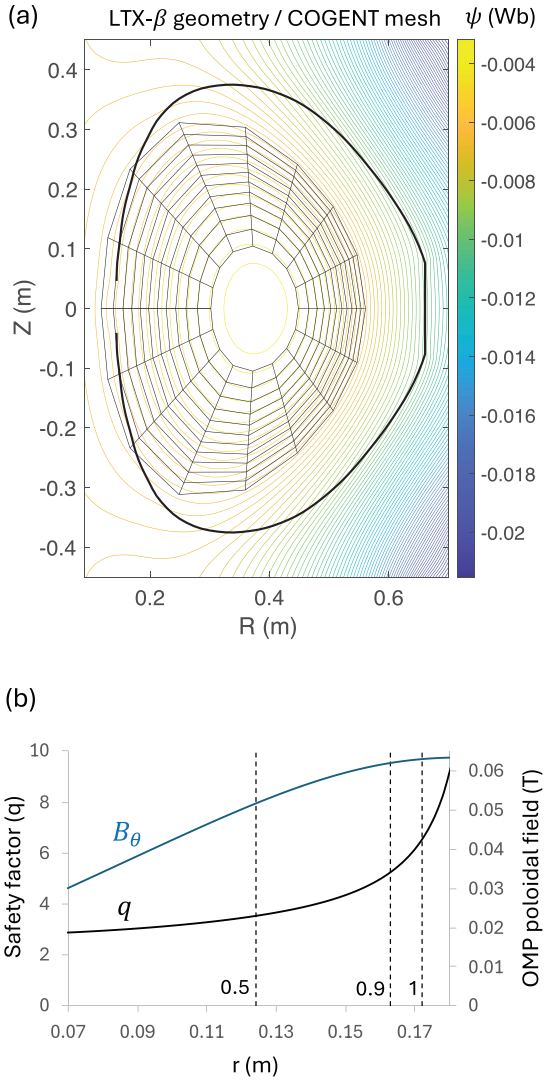

FIG. 1. Magnetic geometry of the COGENT simulations: (a) shows the poloidal flux function together with a coarse version of the flux-aligned computational mesh and the limiter wall (thick black curve) and (b) shows the magnetic safety factor (black) and the outer midplane (OMP) values of the poloidal magnetic field (blue) plotted against the radial distance from the tokamak axis. The simulation domain spans the region of $\psi_N = (0.15; 1.1)$. The vertical dashed lines in Frame (b) illustrate the radial position of the magnetic flux surfaces corresponding to $\psi_N = (0.5, 0.9, 1)$.

The results of numerical simulations employing a hybrid kinetic-ion/fluid electron model in Eqs. (1) and (5) is shown in Figs. 2–4. The boundary conditions for electrostatic potential correspond to a zero-Dirichlet BC at the outer radial boundary and to the consistent BC in Eq. (11) at the inner radial boundary. A locally Maxwellian distribution function, with the ion density and temperature profiles shown in Fig. 2(a) and a zero parallel velocity moment, is used for the initialization and to specify the inflow flux at the radial boundaries. The baseline grid resolution is given by $N_\psi = 44$, $N_\theta = 32$, $N_{v_\parallel} = 64$, and $N_\mu = 49$, and the velocity domain extent corresponds to $-3.25\overline{V}_{Ti}$

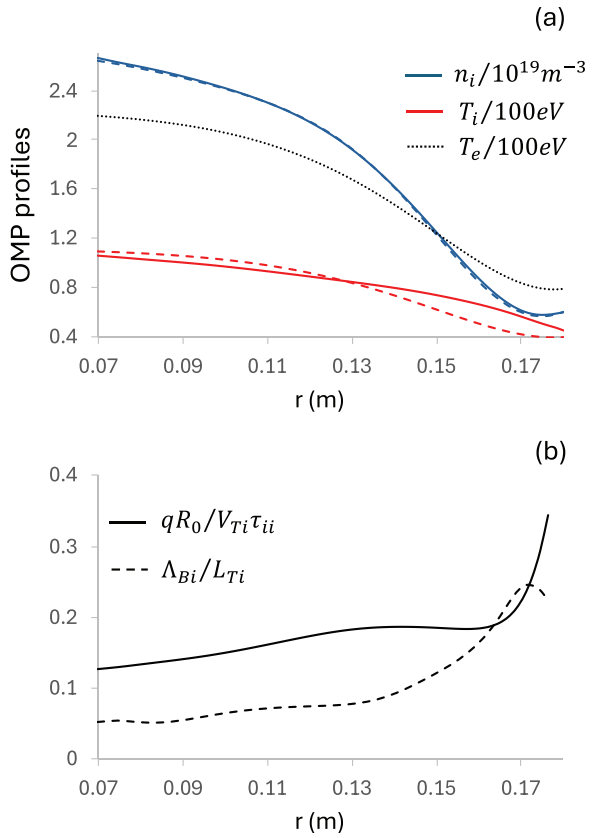

FIG. 2. Simulation results for the hydrogen profiles: (a) shows the OMP profiles for the initial (dashed curves) and final (solid curves) states and (b) illustrates the normalized parameters for the collisionality (solid curve) and the nonlocal effects (dashed curve) obtained for the final state. The dotted curve in frame (a) illustrates the electron temperature profile that is maintained fixed in the simulations. The baseline grid resolution $(N_\psi, N_\theta, N_{v_\parallel}, N_\mu) = (44, 32, 64, 49)$ is used for the simulations.

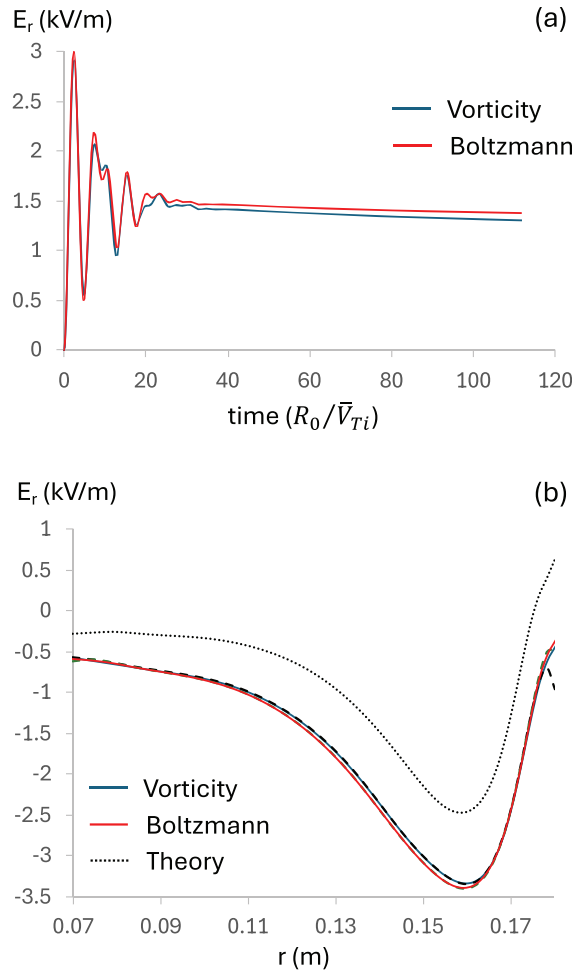

FIG. 3. Simulation results for the radial electric field: (a) shows the time history measured at $r = 0.14$ m (OMP) for the grid resolution given by $(N_\psi, N_\theta, N_{v_\parallel}, N_\mu) = (44, 32, 64, 49)$ and (b) shows the final-state OMP profile for the reference (solid) and higher (dashed) spatial grid resolutions corresponding to (44,32,64,49) and (88,64,64,49), respectively. The results from the hybrid (vorticity) model, shown in blue, are compared with the results from the adiabatic (Boltzmann) electron model, shown in red. The dotted black curve illustrates the simplified theoretical estimate in Eq. (16).

$\leq v_\parallel \leq 3.25\bar{V}_{Ti}$ and $0 \leq \mu \leq 6.3T_0/B_0$, where $\bar{V}_{Ti} = \sqrt{2T_0/m_i}$, $T_0 = 100$ eV, and $m_i = m_p$ is a proton mass. The convergence studies presented in Figs. 3(b) and 4(a) confirm that the baseline grid resolution yields a converged numerical solution.

The simulation is advanced for the short (collisional) time period of $t_{sim} = 112R_0/\bar{V}_{Ti}$, during which the initial transient processes (e.g., GAMs) are relaxed and a quasi-stationary solution is reached [see Fig. 3(a)]. We note that running this simulation for a much longer (transport) timescale and allowing the profile evolution to saturate may result in a compromised solution for the background radial electric field and toroidal rotation, as pointed out in Ref. 29. The quasi-stationary solution for the hydrogen density and temperature is illustrated in Fig. 2(a). While the radial particle flux is quickly suppressed and the density evolution is minimal, difference between the initial and final temperature profiles is more pronounced emphasizing the role of non-local effects measured by Λ_{Bi}/L_{Ti} in Fig. 2(b). Here, $L_{Ti} = T_i(\partial T_i/\partial R)^{-1}$ is the radial length scale for the final hydrogen temperature variations, $\Lambda_{Bi} = \rho_i(B_\phi/B_\theta)\sqrt{r/R_0}$ is the characteristic thermal banana orbit width, $r = R - R_0$ is the minor radius coordinate, and R_0 is the radial coordinate of the magnetic axis. In addition, Fig. 2(b) illustrates the characteristic hydrogen collisionality using the ratio $qR_0/(V_{Ti}\tau_{ii})$, where $\tau_{ii}^{-1} = (4/3)\sqrt{\pi}n_i e^4 m_i^{-1/2} T_i^{-3/2} \ln\Lambda$ is the basic ion–ion collision frequency given by Braginskii.[26] A weakly collisional regime, $qR_0/(V_{Ti}\tau_{ii}) < 1$, is observed across the entire simulation domain.

Figure 4 shows the neoclassical transport power profile in the final state

$$Q = \oint dA \int\int dv_\parallel d\mu \frac{2\pi}{m_i} \dot{R}_\psi \left(\frac{m_i v_\parallel^2}{2} + \mu B + Z_i e\Phi\right) B_\parallel^* f_i. \quad (14)$$

Here, $\dot{R}_\psi$ denotes the projection of the ion drift velocity on the outward radial direction. To assess the role of the collisional model, we

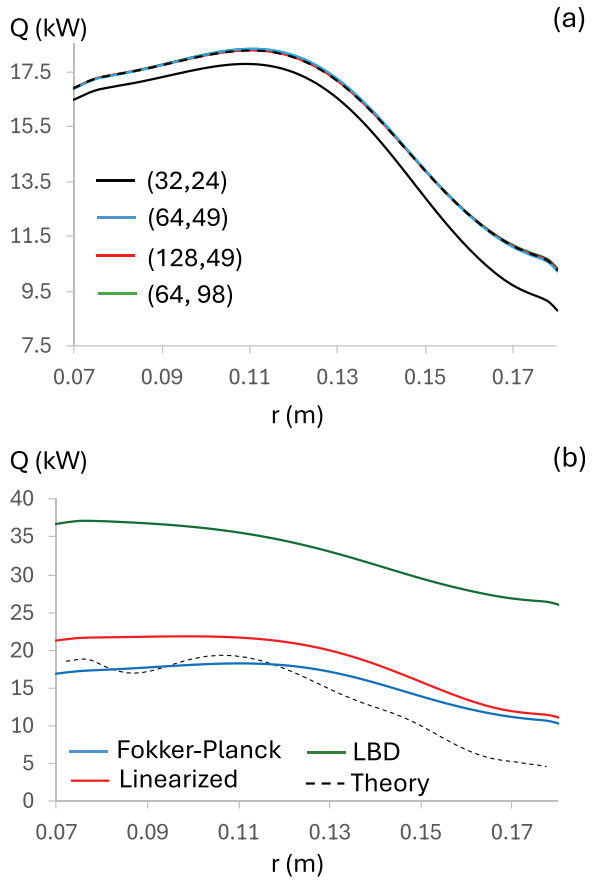

FIG. 4. Simulation results for the hydrogen neoclassical transport power in the final state: Frame (a) illustrates the convergence studies where the bottom black curve corresponds to the explicit simulations with the velocity resolution of $(N_{v_\parallel}, N_\mu) = (32, 24)$ and the virtually indistinguishable top curves correspond to the implicit simulations with $\Delta t = 0.11 R_0/\overline{V}_{Ti}$ and the velocity grid resolutions of (64,49) (128,49) and (64,98). To demonstrate the time integration accuracy, the top curves also include the results of explicit simulations for the baseline resolution (64,49) illustrated by the black dashed curve. The spatial grid resolution corresponds to $(N_\psi, N_\theta) = (44, 32)$. Frame (b) shows the results of the baseline grid resolution $(N_\psi, N_\theta, N_{v_\parallel}, N_\mu) = (44, 32, 64, 49)$ simulations for the different choices of the ion–ion collisional model and compares them with the simplified theoretical estimate in Eq. (15).

present the results of numerical simulations for the full-nonlinear Fokker–Planck operator,[20,21] a model linearized operator,[19,22] and the Lenard–Bernstein/Dougherty (LBD) operator.[23] For the LBD operator, the velocity-independent collision frequency coefficient is given by τ_{ii}^{-1}. It is readily seen that the LBD collision model significantly overpredicts the neoclassical flux. The linearized collision model adopts the initial Maxwellian for the background ion distribution and it agrees with the nonlinear Fokker–Planck models within ∼40%. In addition, the simulation results are compared with a simplified analytical formula derived for a weakly collisional neoclassical ion heat flux in a large aspect ratio circular geometry:[34]

$$q_{NC} = 1.35\varepsilon^{1/2}\frac{B^2}{B_\theta^2}\frac{n_i T_i}{m_i \omega_{ci}^2 \tau_i}\left|\frac{\partial T_i}{\partial R}\right|. \tag{15}$$

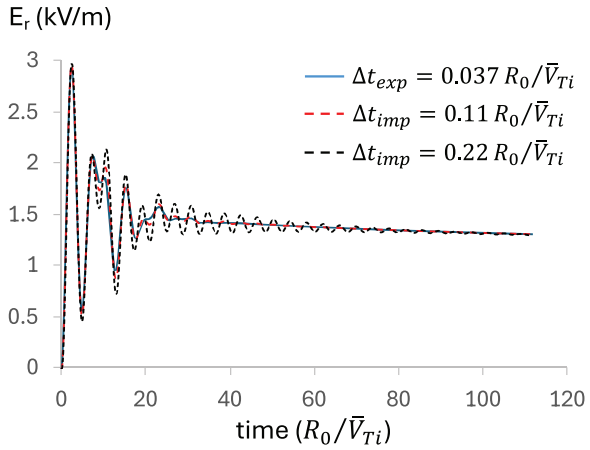

FIG. 5. The results of the explicit (solid) and implicit (dashed) simulations for the radial electric field measured at $r = 0.14$ m (OMP). The baseline grid resolution $(N_\psi, N_\theta, N_{v_\parallel}, N_\mu) = (44, 32, 64, 49)$ is used for the simulations.

The results from the hybrid-model simulations employing the quasi-neutrality equation for the vorticity variable [Eq. (5)] are compared with the counterpart simulations that solve the gyrokinetic Poisson equation [Eq. (7)] coupled with the adiabatic electron response [Eq. (8)]. Both the time dependent evolution and the final quasi-stationary profile for the radial electric field are found to be in good agreement (see Fig. 3). As previously mentioned in Sec. II, the adiabatic electron model in Eqs. (7) and (8) uses the consistent Neumann-like BC at both radial boundaries, in contrast to the vorticity model that is subject to a zero-Dirichlet BC at the outer radial boundary. As a result, a boundary layer may develop near the outer radial boundary in the hybrid-model simulations as seen in Fig. 3(b) for the case where the spatial resolution is increased by a factor of two, i.e., $N_\psi = 88$, $N_\theta = 64$. The layer is apparently formed to mediate the transition from a poloidally uniform (zero) boundary condition to a poloidally non-uniform interior solution that closely follows the poloidal density variations (i.e., the Boltzmann response), as enforced by the last term on the right-hand side of Eq. (5). It is important to note that the numerical solution for the radial electric field is well-converged outside this boundary layer. In addition, the simulation results for the radial electric field are compared with a simplified analytical formula derived for a neocalssical radial electric field in a weakly collisional regime for a large aspect ratio circular geometry:[34]

$$E_\psi^{NC} = \frac{1}{e n_i}\nabla P_i \cdot \mathbf{e}_\psi - \frac{1.17}{e}\nabla T_i \cdot \mathbf{e}_\psi - \frac{B}{B_\phi}\frac{B_\theta V_{i,\parallel}}{c}. \tag{16}$$

Here, $V_{i,\parallel}$, T_i, and P_i are the ion parallel flow velocity, temperature, and pressure, respectively, and B_θ and B_ϕ are the projections of the magnetic field onto the poloidal and toroidal directions.

Finally, we discuss the performance efficiency of our implicit time integration approach for the hybrid-model simulations. The time history of the radial electric field obtained in the "explicit" and "implicit" simulations with the baseline grid resolution is shown in Fig. 5. For both time integration methods, the vorticity equation is advanced using the implicit backward Euler method, and the fixed E-field assumption is applied when advancing the gyrokinetic equation. The

explicit and implicit approaches differ in how they advance the gyrokinetic equation: either using a fourth-order explicit Runge–Kutta (RK4) scheme (explicit approach) or a second-order implicit additive Runge–Kutta (ARK2) scheme (implicit approach). The CFL-limited time step for the explicit simulations is approximately given by $\Delta t_{\exp} = 0.037 R_0/\overline{V}_{Ti} = 0.1\ \mu$s. Due to the presence of diffusive terms in the collision operator, the Fokker–Planck collision model limits the overall time step. However, the CFL-limited time step for the gyrokinetic advection, i.e., the Vlasov operator, is only marginally larger, $\Delta t_{ADV} \approx 2\Delta t_{CLS}$. Two sets of the implicit simulations use time steps of $\Delta t_{imp} = 0.11 R_0/\overline{V}_{Ti} = 3\Delta t_{exp}$ and $\Delta t_{imp} = 0.22 R_0/\overline{V}_{Ti} = 6\Delta t_{exp}$. As mentioned earlier (see Sec. II), the fixed E-field assumption together with the explicit advance of the consistent boundary condition limits the accuracy and stability of the "implicit" simulations discussed here. This becomes apparent from Fig. 5 showing spurious ringing of the numerical solution for $\Delta t_{imp} = 6\Delta t_{exp}$, which however eventually relaxes to the correct steady-state. A further increase in the time step leads to a numerical instability.

Making use of the implicit approach provides the speedup of the baseline-resolution simulations by the factors of 1.4× and 2.6× for the cases of $\Delta t_{imp} = 0.11 R_0/\overline{V}_{Ti}$ and $\Delta t_{imp} = 0.22 R_0/\overline{V}_{Ti}$, respectively, as compared to the explicit simulations. We note that to reduce the computational expense associated with calculating the Rosenbluth potentials in the Fokker–Planck operator and to make it comparable to that of the advection operator (in the explicit case), the Rosenbluth potentials are updated only every ten steps, with virtually no difference observed in the solution. As expected, enhanced speedup is observed in the simulations with 2× higher velocity resolution [shown in Fig. 4(a)] that require 4× smaller time step for the stable explicit time integration. For the case of $\Delta t_{imp} = 0.11 R_0/\overline{V}_{Ti}$ the speedup from using the implicit modeling increases to 6.8×. It is also interesting to note the LBD collision model is observed to impose more severe CFL constraint as compared to the Fokker–Planck model for the same velocity grid resolution. As a result, a speedup of 4.6× is observed in the simulations with the LBD collision and the baseline grid resolution [see Fig. 4(b)] when using $\Delta t_{imp} = 0.11 R_0/\overline{V}_{Ti}$. Finally, we mention that the COGENT simulations are run on the Dane cluster of the Lawrence Livermore National Laboratory (LLNL) HPC system.[35] The baseline-grid simulations use 224 cores and require approximately 8.5 min of wall time for the implicit calculations with the Fokker–Planck collision model and $\Delta t_{imp} = 0.22 R_0/\overline{V}_{Ti}$.

IV. SIMULATIONS OF THE LITHIUM NEOCLASSICAL TRANSPORT

The full-F neoclassical transport modeling of the lithium impurity species assumes the trace limit and utilizes the fixed background solution for the hydrogen species, along with the electrostatic potential variations obtained in Sec. III. The model linearized multi-species collision operator developed in Ref. 25 is employed to describe the collisions between the lithium and hydrogen species. The background Maxwellian distribution functions used for linearization of the lithium and hydrogen species in the collision model are assumed to share the hydrogen temperature and a zero parallel velocity moment. Under these assumptions, the collisional operator is consistent with the Sugama model.[36] The goal of the present studies is to obtain a steady-state transport solution for the lithium species consistent with the zero lithium particle source inside the simulation domain. To compensate for the fact that the COGENT simulation domain cannot be extended all the way to the magnetic axis, the total (i.e., flux-surface integrated) zero particle flux boundary condition in Eq. (10) is used at both radial boundaries. Due to the presence of strong collisional exchange in energy and parallel momentum between the lithium and hydrogen species, particular boundary values of the total angular momentum and energy fluxes carried by the lithium may be of lesser importance, and we arbitrarily set them to zero. We note that nearly the same shape of the steady-state lithium density was obtained in simulations with a prescribed Maxwellian inflow BC at the outer radial boundary and a zero-flux BC at the inner radial boundary.

The fully ionized ($Z = 3$) lithium species is initialized with a local Maxwellian distribution, which has the background hydrogen temperature, a zero parallel flow, and a poloidally uniform density $n^0_{Li} = \overline{n}(0.25 \times (\tanh((0.5 - \psi_N)/0.2)) + 0.75)$, where $\overline{n}$ is an arbitrary constant. Two choices for the grid resolution are used to investigate numerical convergence: the baseline $(N_\psi, N_\theta, N_{v_\parallel}, N_\mu) = (44, 32, 64, 49)$ and the coarse-velocity resolution (44, 32, 32, 28). For each case, the background hydrogen distribution and the potential profile are specified as the quasi-stationary (final) solutions of the corresponding hydrogen simulations described in Sec. III. The lithium velocity domain extent is given by $-3.25\overline{V}_{TZ} \le v_\parallel \le 3.25\overline{V}_{TZ}$ and $0 \le \mu \le 6.3 T_0/B_0$, where $\overline{V}_{TZ} = \sqrt{2T_0/m_Z}$, $T_0 = 100$ eV, $B_0 = 3$ kG, and $m_Z = 6.94 m_p$ is the lithium atomic mass.

The steady-state solutions for the lithium density and temperature are shown in Figs. 6 and 7. Saturation of the density profile evolution [see Fig. 8(a)] is consistent with vanishing of the normalized particle flux [see Figs. 8(b) and 8(c)],

$$\Gamma_N = \quad \overline{\Gamma}^{-1} \oint dA \int\int dv_\parallel d\mu \frac{2\pi}{m_Z} \dot{R}_\psi B^*_{\parallel Z} f_Z, \tag{17}$$

where $\overline{\Gamma} = (\overline{\rho}_Z^2/a^2)\overline{n}\overline{V}_{Ti}S$ is the normalization coefficient, $a = 18$ cm is the minor radius, $\overline{\rho}_Z = \overline{V}_{TZ} m_Z c/(ZeB_0) = 4$ mm is the characteristic gyroradius of a lithium ion, and $S = 2.4\ \mathrm{m}^2$ is the flux-surface area measured at the middle of the simulation domain. The final lithium density profile can be elucidated by analyzing the radial force balance equation for the lithium species,

$$\frac{Ze}{c} n(\mathbf{V}_f \times \mathbf{B}) \cdot \mathbf{e}_\psi + Zen\mathbf{E} \cdot \mathbf{e}_\psi - \nabla P_\perp \cdot \mathbf{e}_\psi = 0, \tag{18}$$

where the flow velocity is specified by

$$n\mathbf{V}_f = \frac{2\pi}{m} \int dv_\parallel d\mu \dot{\mathbf{R}} f B^*_\parallel - \frac{c}{Ze} \nabla \times \frac{2\pi}{m} \int dv_\parallel d\mu \mathbf{b} \mu f B^*_\parallel, \tag{19}$$

$P_\perp = (2\pi/m) \int dv_\parallel d\mu (\mu/B) f B^*_\parallel$, and we suppressed the subscript denoting lithium ions to simplify notation. Note that the first term on the RHS of Eq. (19) corresponds to the flow of guiding centers and the second term, representing the curl of the plasma magnetization, describes the diamagnetic flow.[37] Figure 9 illustrates the physical terms in Eq. (18). In the absence of strong toroidal rotation sources, the simulations show close balance between the lithium pressure gradient term and the background radial electric field. This result, along with similar values for the hydrogen and lithium temperatures, $T_{Li} \sim T_H$ [see Fig. 6(b)] leads to the relation $\partial(n_{Li}T_H)/\partial r \sim Z_{Li} e n_{Li} E_r$. Stronger variations in the lithium density, as compared to the hydrogen density, are now explained by the higher value of the lithium charge state, $Z_{Li} = 3$.

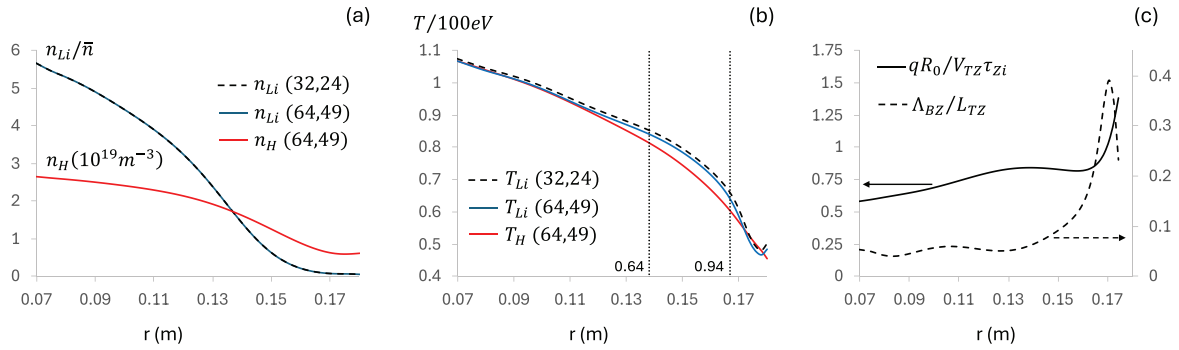

FIG. 6. The steady-state lithium OMP profiles of the (a) density, (b) temperature, and (c) the normalized banana width and collisionality for the baseline grid resolution parameters $(N_\psi, N_\theta, N_{v_\parallel}, N_\mu) = (44, 32, 64, 49)$. Frames (a) and (b) also show solutions (dashed curves) obtained with the coarse velocity grid resolution $(N_{v_\parallel}, N_\mu) = (32, 24)$. The hydrogen density and temperature profiles measured in the final quasi-stationary state of the hydrogen neoclassical simulations [see Fig. 2(a)] are shown for comparison in frames (a) and (b). The vertical dotted lines in frame (b) illustrate the radial position of the magnetic flux surfaces corresponding to $\psi_N = (0.64, 0.94)$, where the poloidal asymmetries are analyzed.

Figure 9 also illustrates the sum of all terms on the RHS of Eq. (18), which are found to be in very close balance. It is, however, instructive to note that the long-wavelength limit of the gyrokinetic equation inherently enforces perpendicular force balance as part of its formulation. Indeed, evaluating the ion flow in Eq. (19) by making use of Eq. (2), we obtain

$$n\mathbf{V}_f = nV_\parallel \mathbf{b} + cn\frac{\mathbf{E}\times\mathbf{b}}{B} + c\frac{P_\parallel}{ZeB}\nabla\times\mathbf{b} + c\frac{P_\perp}{ZeB^2}\mathbf{b}\times\nabla B - \frac{c}{Ze}\nabla\times\left(\mathbf{b}\frac{P_\perp}{B}\right), \tag{20}$$

where $\{V_\parallel, P_\parallel\} = (2\pi/m)\int dv_\parallel d\mu \left\{n^{-1}v_\parallel, mv_\parallel^2\right\} f B_\parallel^*$. In deriving Eq. (20), we neglected the small difference between $B_\parallel^*$ and B in the velocity moments calculation. The difference is of the order of $(\rho_i/L_B)B$ and would only contribute to second-order corrections in the perpendicular force balance. Introducing the magnetic field curvature $\boldsymbol{\kappa}$ and making use of $\nabla\times\mathbf{b} = \mathbf{b}\mathbf{b}\cdot\nabla\times\mathbf{b} + \mathbf{b}\times\boldsymbol{\kappa}$, we readily obtain

$$\frac{Ze}{c}n\mathbf{V}_f\times\mathbf{B} + Zen\mathbf{E}_\perp - \nabla_\perp P_\perp - (P_\parallel - P_\perp)\boldsymbol{\kappa} = 0. \tag{21}$$

Apart from the pressure anisotropy corrections, Eq. (21) is consistent with the simplified force balance in Eq. (18).

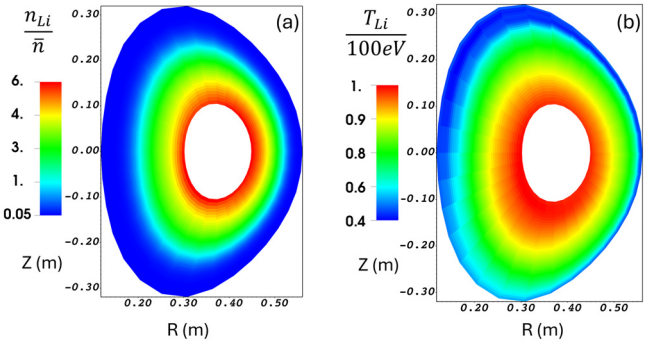

FIG. 7. The steady-state lithium profiles of the (a) density and (b) temperature. The baseline grid resolution $(N_\psi, N_\theta, N_{v_\parallel}, N_\mu) = (44, 32, 64, 49)$ is used for the simulation.

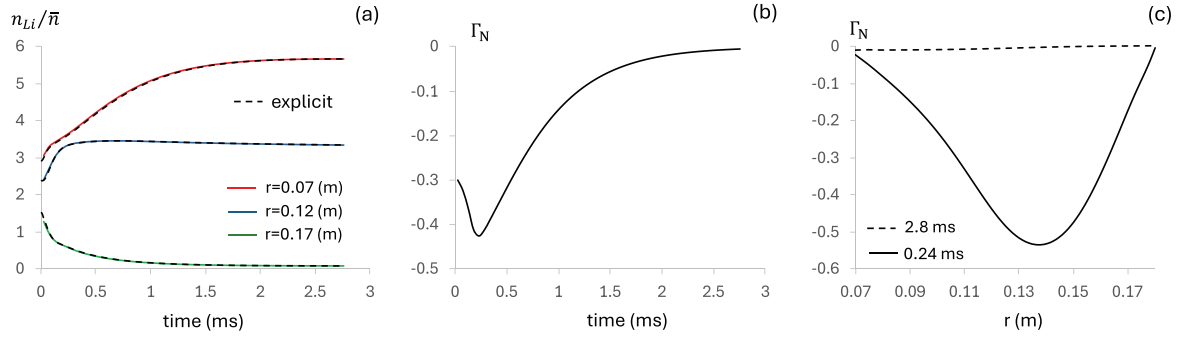

FIG. 8. Particle transport properties in the lithium neoclassical simulations: (a) shows the time history of the normalized density measured at various radial locations in the implicit (solid) and explicit (dashed) simulations, (b) shows the time history of the total radial particle flux in Eq. (17) measured at $r = 0.12$ m, and (c) shows the radial profile of the total particle flux measured at $t = 0.24$ ms (solid) and $t = 2.8$ ms (dashed).

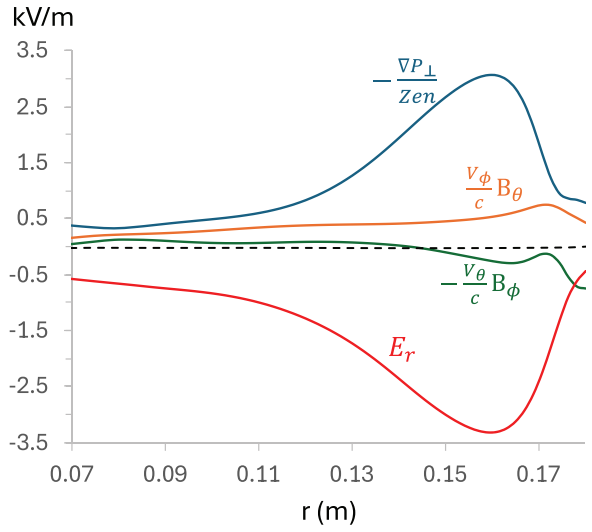

FIG. 9. Radial force balance terms [see Eq. (18)] for the lithium species measured in the final steady state. The dashed curve illustrates the sum of all terms on the LHS of Eq. (18). The baseline grid resolution $(N_\psi, N_\theta, N_{v_\parallel}, N_\mu) = (44, 32, 64, 49)$ is used for the simulation.

It is important to investigate the role of non-local effects and impurity poloidal asymmetries, which may become pronounced in the outer-core region characterized by steeper background gradients. Poloidal density asymmetries in impurity species are routinely measured in tokamaks and can be used for numerical model validation. Figure 6(c) illustrates the characteristic measure of the non-local effects, Λ_{BZ}/L_{TZ}, and the lithium collisionality, $qR_0/(V_{TZ}\tau_{Zi})$ in the final steady-state. Here, $\Lambda_{BZ} = \rho_Z(B_\phi/B_\theta)\sqrt{r/R_0}$ and $\tau_{Zi}^{-1} = (m_i/m_Z)(4/3)\sqrt{2\pi}n_i Z^2 e^4 m_i^{-1/2} T_i^{-3/2} \ln\Lambda$. Note that the increase in the value of Λ_{BZ}/L_{TZ} in the region $r > 0.13$ m is consistent with an increased deviation in the hydrogen and lithium temperatures. The relative poloidal variations in the lithium density and temperature are also found to increase toward the outer core region. Measured by the ratio of a maximum to a minimum value within the same flux surface, the poloidal variations in the lithium density (temperature) increase from 1.10 (1.1) to 1.3 (1.5) when evaluated at $\psi_N = 0.64$ and $\psi_N = 0.94$, respectively. For comparison, the poloidal variations in the hydrogen density and temperature evaluated at $\psi_N = 0.94$ are given by 1.05 and 1.25, respectively.

We now examine the performance efficiency of our implicit time integration approach for lithium transport simulations. With the electric field held fixed in the trace-impurity limit, the fully implicit simulations are expected to achieve second-order time integration accuracy, employing an ARK2 scheme for advancing the gyrokinetic equation in time. Figure 8(a) shows excellent agreement between the results of implicit and explicit simulations for the coarse velocity resolution case. The explicit simulations use an RK4 scheme with the stable time step, $\Delta t_{\exp} = 0.125\ \mu$s, limited by the stiff collision term. The implicit simulations use $\Delta t_{imp} = 5\ \mu s = 40\Delta t_{exp}$ and demonstrate a 6× speedup. In contrast to the limited stability of the hydrogen transport IMEX simulations, the fully implicit lithium simulations are stable for any value of the time step. However, the efficiency of the multi-physics preconditioning approach, which relies on the operator-splitting approximation, degrades as Δt_{imp} increases. In the present simulations, about 10 preconditioned GMRES iterations are required to achieve a relative tolerance of 1.0×10^{-3}. The baseline-grid simulations use the same implicit time step $\Delta t_{imp} = 5\ \mu$s, which is about 160× larger than the stable time step for the corresponding explicit simulations. The implicit calculations require about 20 preconditioned GMRES iterations to achieve a relative tolerance of 1.0×10^{-3} and provide an 14× speedup. For comparison, only three preconditioned GMRES iterations are needed to achieve the same tolerance when inverting the collision and Vlasov operators separately. The baseline (coarse velocity) resolution simulations use 224 (64) cores of the LLNL Dane cluster[35] and require approximately 23 (8.3) min of wall time per 1 ms of physical time for the implicit time integration approach.

Finally, we comment on the role of anomalous transport in impurity simulations. Anomalous transport is driven by microturbulence perturbations and can significantly impact the impurity accumulation process, which occurs on a long (transport) timescale. To assess its influence, an *ad hoc* radial transport model is used in 4D (axisymmetric) COGENT simulations.[8] A general version of this model, which can reproduce the particle and energy anomalous transport matrix commonly used in fluid simulations, is described in detail elsewhere.[38] In the present work, we employ a simplified form by introducing the following radial diffusion term to the right-hand side of Eq. (1)

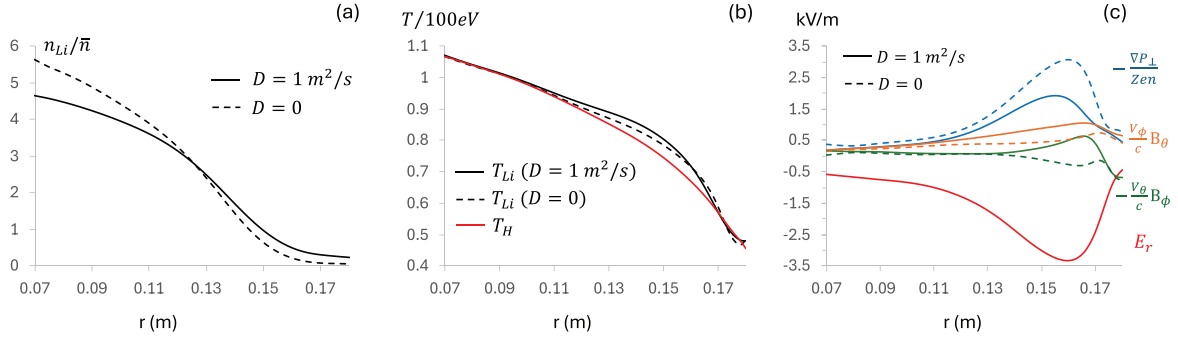

FIG. 10. Role of anomalous transport in trace impurity simulations. The frames show the steady-state OMP profiles of the lithium density (a), temperature (b), and contributions to the radial force balance (c). The results from the simulations without anomalous transport (shown in Figs. 6 and 8) are illustrated in frames (a)–(c) with the dashed curves. Frame (b) also shows the hydrogen temperature profile (red curve). The baseline grid resolution $(N_\psi, N_\theta, N_{v_\parallel}, N_\mu) = (44, 32, 64, 49)$ is used in all simulations.

$$T_{AN}\left(B_{\parallel i}^{*} f_i\right) = \nabla \cdot \left(D_{AN} \nabla_{\psi}\left(B_{\parallel i}^{*} f_i\right)\right). \quad (22)$$

Here, $\nabla_{\psi} \equiv \mathbf{e}_{\psi}(\mathbf{e}_{\psi} \cdot \nabla)$ denotes the radial gradient operator, and the diffusion coefficient is taken as $D_{AN} = 1.0\,\mathrm{m}^2\,\mathrm{s}^{-1}$. The operator in Eq. (22) is evaluated subject to a zero-flux boundary condition, $\nabla_{\psi}(B_{\parallel i}^{*} f_i) = 0$, imposed at the radial boundaries. The results of the lithium simulations, including the *ad hoc* anomalous transport model, are shown in Fig. 10 for the case of the baseline grid resolution. As expected, the presence of the radial diffusion term relaxes the lithium profile gradients and mitigates impurity accumulation [see Fig. 10(a)]. Measured by the ratio of the outer midplane lithium density computed at the inner (core) and outer (edge) radial boundaries, the accumulation factor drops from $n_{Li}^{core}/n_{Li}^{edge} \approx 100$ to $n_{Li}^{core}/n_{Li}^{edge} \approx 20$ when anomalous transport effects are added. We also note that the decrease in the lithium pressure gradient force due to anomalous particle transport is compensated by an increased $V \times B$ contribution to the radial force balance [see Fig. 10(c)].

For the numerical simulation illustrated in Fig. 10, the implicit time step $\Delta t_{imp} = 5\,\mu s$ is about 1.5× larger than the CFL-limited time step for the anomalous transport operator. Although a suitable preconditioner for phase-space diffusion is not currently available in COGENT, the operator in Eq. (22) is nevertheless included as an implicit term in the IMEX formulation. As a result, a 1.35× slowdown in the simulations is observed. Developing an effective preconditioner for phase-space diffusion will be the subject of our future work.

V. CONCLUSIONS

In this paper, we report the development and application of implicit time integration capabilities for axisymmetric full-F continuum simulations of neoclassical ion transport using COGENT. The numerical model is applied to the transport simulations of the main ion (hydrogen) and impurity (lithium) species in the closed-field-line region of the LTX-β experiment. The hydrogen species simulations are performed on a collisional timescale to obtain neoclassical transport fluxes and self-consistent electrostatic potential variations corresponding to a plasma background profile characteristic of LTX-β. This quasi-stationary hydrogen solution is then used to perform lithium simulations on a transport timescale under the trace-limit approximation. The hydrogen simulations employ the hybrid kinetic-ion/fluid-electron model and consider three ion–ion collision models in order to assess the role of a collision operator in a weakly collisional transport regime. These models include the full-nonlinear Fokker–Planck operator, a model linearized operator, and the Lenard–Bernstein/Dougherty (LBD) operator. The simulations demonstrate moderate (∼40%) over-prediction of neoclassical transport power by the linearized model and significant over-prediction (∼150%) by the LBD model.

The lithium simulations employ a model multi-species linearized collision operator to describe interaction with the fixed hydrogen background. Lithium profiles are evolved until a steady-state transport solution consistent with a zero lithium particle source is obtained. To compensate for the limited COGENT simulation domain, which does not extend to the magnetic axis, a zero-flux boundary condition is imposed. The simulations reveal substantial accumulation of impurity species in the core region, $n_{Li}^{core}/n_{Li}^{edge} \approx 100$, which is elucidated by analyzing the radial force balance in the final state. In the absence of an external source of toroidal momentum, as assumed in the present model, the radial force balance is found to be dominated by the electrostatic and the pressure-gradient forces, $\partial n_{Li} T_{Li}/\partial r \sim Z_{Li} e n_{Li} E_r$. Collisional energy exchange between lithium and hydrogen leads to similar temperatures $T_{Li} \sim T_H$. Consequently, steeper lithium density variations are required to maintain force balance due to its larger charge state ($Z_{Li} = 3$). Including the effects of anomalous transport, modeled via an *ad hoc* radial diffusion term with $D_{AN} = 1.0\,\mathrm{m}^2\,\mathrm{s}^{-1}$, is observed to relax the lithium density profile and reduce the core accumulation factor to $n_{Li}^{core}/n_{Li}^{edge} \approx 20$. Additionally, poloidal impurity asymmetries are examined. The poloidal variations increase with the strength of non-local effects and reach approximately 30% and 50% in the near-edge density and temperature profiles, respectively.

The use of implicit time integration enables a substantial speedup in the numerical simulations. In the hydrogen simulations that employ the fixed E-field approximation during the time step evolution of the gyrokinetic equation, the stable implicit time step size is limited by collective processes such as geodesic acoustic modes (GAMs). Nevertheless, higher-velocity-resolution simulations with the Fokker–Planck operator achieve a speedup of approximately 7×. In the trace-limit lithium simulations, which assume a fixed electrostatic potential, there is no stability limit on the time step. However, the performance of the multi-physics preconditioner, based on an operator-splitting approach, may degrade as Δt increases. Baseline velocity resolution implicit simulations, using a time step 160× larger than the CFL-limited explicit stable time step, demonstrate a speedup of 14×.

Finally, we note that for the case of the LTX-β core region modeled here, the Courant-limited time steps corresponding to the advection and collision operators are of the same order. As a result, the efficiency of the global multi-physics preconditioner, which is constructed by using an operator-split approach, may be limited. Larger speed-up factors relative to explicit simulations can be expected when modeling physical systems in which stiffness is dominated by a single process, such as strong ion–ion collisions in cold plasma regions near divertor plates. Our future work will explore the performance of the implicit kinetic capabilities in COGENT for edge plasma modeling in divertor geometries, including simulations of lithium transport for the upcoming NSTX-U facility.

ACKNOWLEDGMENTS

The authors thank the LTX-β team for providing the magnetic equilibrium data. This research was supported by the U.S. Department of Energy under Contract No. DE-AC52-07NA27344.

AUTHOR DECLARATIONS

Conflict of Interest

The authors have no conflicts to disclose.

Author Contributions

M. Dorf: Conceptualization (equal); Formal analysis (lead); Methodology (equal); Software (equal). **M. Dorr:** Methodology (equal); Software (equal). **D. Ghosh:** Methodology (equal); Software (equal). **M. Umansky:** Conceptualization (equal); Formal analysis (supporting). **V. Soukhanovskii:** Conceptualization (equal); Formal analysis (supporting).

DATA AVAILABILITY

The data that support the findings of this study are available from the corresponding author upon reasonable request.

REFERENCES

[1]C. S. Chang, S. Ku, A. Loarte, V. Parail, F. Köchl, M. Romanelli, R. Maingi, J.-W. Ahn, T. Gray, J. Hughes, B. LaBombard, T. Leonard, M. Makowski, and J. Terry, "Gyrokinetic projection of the divertor heat-flux width from present tokamaks to ITER," Nucl. Fusion **57**, 116023 (2017).

[2]P. Ulbl, T. Body, W. Zholobenko, A. Stegmeir, J. Pfennig, and F. Jenko, "Influence of collisions on the validation of global gyrokinetic simulations in the edge and scrape-off layer of TCV," Phys. Plasmas **30**, 052507 (2023).

[3]N. R. Mandell, A. Hakim, G. W. Hammett, and M. Francisquez, "Electromagnetic full-f gyrokinetics in the tokamak edge with discontinuous Galerkin methods," J. Plasma Phys. **86**, 905860109 (2020).

[4]M. Dorf and M. Dorr, "Continuum gyrokinetic simulations of edge plasmas in single-null geometries," Phys. Plasmas **28**, 032508 (2021).

[5]Z. Lin and L. Chen, "A fluid–kinetic hybrid electron model for electromagnetic simulations," Phys. Plasmas **8**, 1447–1450 (2001).

[6]Y. Chen and S. Parker, "A gyrokinetic ion zero electron inertia fluid electron model for turbulence simulations," Phys. Plasmas **8**, 441–446 (2001).

[7]R. Hager, J. Lang, C. S. Chang, S. Ku, Y. Chen, S. E. Parker, and M. F. Adams, "Verification of long wavelength electromagnetic modes with a gyrokinetic-fluid hybrid model in the XGC code," Phys. Plasmas **24**, 054508 (2017).

[8]M. Dorf and M. Dorr, "Continuum kinetic modelling of cross-separatrix plasma transport in a tokamak edge including self-consistent electric fields," Contrib. Plasma Phys. **58**, 434–444 (2018).

[9]M. Dorf and M. Dorr, "Modelling of electrostatic ion-scale turbulence in divertor tokamaks with the gyrokinetic code COGENT," Contrib. Plasma Phys. **62**, e202100162 (2022).

[10]See http://www.llnl.gov/casc/hypre/ for "HYPRE: Scalable Linear Solvers and Multigrid Methods."

[11]T. A. Manteuffel, J. Ruge, and B. S. Southworth, "Nonsymmetric algebraic multigrid based on local approximate ideal restriction (IAIR)," SIAM J. Sci. Comput. **40**, A4105–A4130 (2018).

[12]T. A. Manteuffel, S. Munzenmaier, J. Ruge, and B. Southworth, "Nonsymmetric reduction-based algebraic multigrid," SIAM J. Sci. Comput. **41**, S242–S268 (2019).

[13]D. Boyle, J. Anderson, S. Banerjee, R. Bell, W. Capecchi, D. Elliott, C. Hansen, S. Kubota, B. LeBlanc, A. Maan, R. Maingi, R. Majeski, J. Menard, S. Oliva, T. Rhodes, V. Soukhanovskii, and L. Zakharov, "Extending the low-recycling, flat temperature profile regime in the lithium tokamak experiment-β (LTX-β) with ohmic and neutral beam heating," Nucl. Fusion **63**, 056020 (2023).

[14]A. Maan, D. P. Boyle, R. Majeski, G. J. Wilkie, M. Francisquez, S. Banerjee, R. Kaita, R. Maingi, B. P. LeBlanc, S. Abe, E. Jung, E. Perez, W. Capecchi, E. T. Ostrowski, D. B. Elliott, C. Hansen, S. Kubota, V. Soukhanovskii, and L. Zakharov, "Estimates of global recycling coefficients for LTX-β discharges," Phys. Plasmas **31**, 022505 (2024).

[15]S. Satake, Y. Idomura, H. Sugama, and T.-H. Watanabe, "Benchmark test of drift-kinetic and gyrokinetic codes through neoclassical transport simulations," Comput. Phys. Commun. **181**, 1069–1076 (2010).

[16]T. Vernay, S. Brunner, L. Villard, B. F. McMillan, S. Jolliet, T. M. Tran, A. Bottino, and J. P. Graves, "Neoclassical equilibria as starting point for global gyrokinetic microturbulence simulations," Phys. Plasmas **17**, 122301 (2010).

[17]G. Dif-Pradalier, P. H. Diamond, V. Grandgirard, Y. Sarazin, J. Abiteboul, X. Garbet, P. Ghendrih, G. Latu, A. Strugarek, S. Ku, and C. S. Chang, "Neoclassical physics in full distribution function gyrokinetics," Phys. Plasmas **18**, 062309 (2011).

[18]M. Landreman and D. R. Ernst, "Local and global Fokker–Planck neoclassical calculations showing flow and bootstrap current modification in a pedestal," Plasma Phys. Controlled Fusion **54**, 115006 (2012).

[19]M. A. Dorf, R. H. Cohen, M. Dorr, T. Rognlien, J. Hittinger, J. Compton, P. Colella, D. Martin, and P. McCorquodale, "Simulation of neoclassical transport with the continuum gyrokinetic code COGENT," Phys. Plasmas **20**, 012513 (2013).

[20]M. A. Dorf, R. H. Cohen, M. Dorr, J. Hittinger, and T. D. Rognlien, "Progress with the COGENT edge kinetic code: Implementing the Fokker-Planck collision operator," Contrib. Plasma Phys. **54**, 517–523 (2014).

[21]D. Ghosh, M. A. Dorf, M. R. Dorr, and J. A. F. Hittinger, "Kinetic simulation of collisional magnetized plasmas with semi-implicit time integration," J. Sci. Comput. **77**, 819–849 (2018).

[22]I. G. Abel, M. Barnes, S. C. Cowley, W. Dorland, and A. A. Schekochihin, "Linearized model Fokker–Planck collision operators for gyrokinetic simulations. I. Theory," Phys. Plasmas **15**, 122509 (2008).

[23]J. P. Dougherty, "Model Fokker-Planck equation for a plasma and its solution," Phys. Fluids **7**, 1788–1799 (1964).

[24]M. Francisquez, J. Juno, A. Hakim, G. W. Hammett, and D. R. Ernst, "Improved multispecies Dougherty collisions," J. Plasma Phys. **88**, 905880303 (2022).

[25]A. R. Knyazev, M. Dorf, and S. I. Krasheninnikov, "Implementation and verification of a model linearized multi-species collision operator in the COGENT code," Comput. Phys. Commun. **291**, 108829 (2023).

[26]S. I. Braginskii, "Transport processes in a plasma," Rev. Plasma Phys. **1**, 205 (1965).

[27]Y. Asahi, V. Grandgirard, Y. Idomura, X. Garbet, G. Latu, Y. Sarazin, G. Dif-Pradalier, P. Donnel, and C. Ehrlacher, "Benchmarking of flux-driven full-F gyrokinetic simulations," Phys. Plasmas **24**, 102515 (2017).

[28]G. Merlo, J. Dominski, A. Bhattacharjee, C. S. Chang, F. Jenko, S. Ku, E. Lanti, and S. Parker, "Cross-verification of the global gyrokinetic codes GENE and XGC," Phys. Plasmas **25**, 062308 (2018).

[29]F. I. Parra and P. J. Catto, "Limitations of gyrokinetics on transport time scales," Plasma Phys. Controlled Fusion **50**, 065014 (2008).

[30]M. A. Dorf, R. H. Cohen, A. N. Simakov, and I. Joseph, "On the applicability of the standard approaches for evaluating a neoclassical radial electric field in a tokamak edge region," Phys. Plasmas **20**, 082515 (2013).

[31]M. Dorf, M. Dorr, and D. Ghosh, "Development of an implicit electromagnetic capability for a hybrid gyrokinetic ion-fluid electron model," Contrib. Plasma Phys. **64**, e202300114 (2024).

[32]Y. Saad, *Iterative Methods for Sparse Linear Systems*, 2nd ed. (Society for Industrial and Applied Mathematics, 2003).

[33]C. Hansen, D. P. Boyle, J. C. Schmitt, and R. Majeski, "Equilibrium reconstruction with 3D eddy currents in the lithium tokamak experiment," Phys. Plasmas **24**, 042513 (2017).

[34]P. Helander and D. J. Sigma, *Collisional Transport in Magnetized Plasmas* (Cambridge University Press, Cambridge, 2002), pp. 195–197.

[35]See https://hpc.llnl.gov for "Livermore Computing: HPC at LLNL."

[36]H. Sugama, T.-H. Watanabe, and M. Nunami, "Linearized model collision operators for multiple ion species plasmas and gyrokinetic entropy balance equations," Phys. Plasmas **16**, 112503 (2009).

[37]R. D. Hazeltine and J. D. Meiss, *Plasma Confinement* (Addison-Wesley, Reading, MA, 1992), pp. 144–145.

[38]J. R. Angus, "On anomalous plasma transport in the edge of magnetic confinement devices," Ph.D. thesis (University of California, San Diego, 2012).